

Influence of Nitrogen Doping on Oxygen Reduction Electrocatalysis at Carbon Nanofiber Electrodes

Stephen Maldonado and Keith J. Stevenson*

Department of Chemistry and Biochemistry, Center for Nano- and Molecular Science and Technology, Texas Materials Institute, The University of Texas at Austin, Austin, Texas 78712

Received: December 7, 2004; In Final Form: December 21, 2004

Nondoped and nitrogen-doped (N-doped) carbon nanofiber (CNF) electrodes were prepared via a floating catalyst chemical vapor deposition (CVD) method using precursors consisting of ferrocene and either xylene or pyridine to control the nitrogen content. Structural and compositional differences between the nondoped and N-doped varieties were assessed using TEM, BET, Raman, TGA, and XPS. Electrochemical methods were used to study the influence of nitrogen doping on the oxygen reduction reaction (ORR). The N-doped CNF electrodes demonstrate significant catalytic activity toward oxygen reduction in aqueous KNO₃ solutions at neutral to basic pH. Electrochemical data are presented which indicate that the ORR proceeds by the peroxide pathway via two successive two-electron reductions. However, for N-doped CNF electrodes, the reduction process can be treated as a catalytic regenerative process where the intermediate hydroperoxide (HO₂[−]) is chemically decomposed to regenerate oxygen, $2\text{HO}_2^- \rightleftharpoons \text{O}_2 + 2\text{OH}^-$. The proposed electrocatalysis mechanisms for ORR at both nondoped and N-doped varieties are supported by electrochemical simulations and by measured difference in hydroperoxide decomposition rate constants. Remarkably, ~100 fold enhancement for hydroperoxide decomposition is observed for N-doped CNFs, with rates comparable to the best known peroxide decomposition catalysts. Collectively the data indicate that exposed edge plane defects and nitrogen doping are important factors for influencing adsorption of reactive intermediates (i.e., superoxide, hydroperoxide) and for enhancing electrocatalysis for the ORR at nanostructured carbon electrodes.

Introduction

While traditional active carbons (carbon black, Vulcan XC-72) demonstrate requisite characteristics of a good catalyst support,¹ they generally exhibit poor inherent catalytic activity for many technologically relevant reactions, particularly for the oxygen reduction reaction (ORR).^{2,3} The ORR occurring in acidic and alkaline solutions at low and moderate temperatures is a topic of tremendous interest in the field of electrocatalysis, chiefly in fuel cells,⁴ metal–air batteries,⁵ and air-breathing cathodes.⁶ Historically, several methods have been used to modify the carbon supports in an effort to improve electrocatalytic performance. Besides optimization of morphological properties (e.g., surface area and porosity), chemical modification of the carbon surface has been explored to stabilize catalyst–support interactions. For instance, carbon-containing oxygen or nitrogen heteroatom functional groups can be prepared via chemical pretreatments with reactive species such as HNO₃, NH₃, or HCN.^{7–11} These pretreatments, however, generally produce carbon–heteroatom functionalities (e.g., hydroxyls, carboxyls, amines) that are unstable under typical catalysis conditions. Other more viable routes entail the dispersion of typically iron or cobalt containing N₄-macrocycles (e.g., porphyrins and phthalocyanines) on high surface area carbons.¹² While these modified carbons demonstrate improved catalytic activity for ORR, the corrosion resistance is poor when used under operational catalysis conditions.¹³ Janke et al.¹⁴ found that more stable, but less active, ORR catalysts could be formed by subjecting carbon-supported transition-metal-centered N₄-mac-

rocycles to extended heat treatments (>800 °C) in inert atmospheres, such as Ar and N₂. Yeager,^{2,15} Dodelet,^{16,17} and Savinell¹⁸ later demonstrated that the specific nature of the precursor was unimportant, as long as the pyrolysis mixture contained carbon along with nitrogen and iron or cobalt.

Despite decades of research on oxygen reduction catalysts consisting of carbon, nitrogen, and transition metal (predominantly iron or cobalt), their ORR mechanistic steps are poorly understood. While nitrogen has been generally identified as an essential element for catalytic activity, poor surface and electrochemical characterizations of these materials and of the ORR process have led to several conflicting views on the specific identity/stoichiometry/composition of the active site. The broad range of methodologies and materials employed to produce active oxygen reduction catalysts makes it extremely difficult to discern controlling parameters for preparing active catalysts. Specifically, the widely variable properties (i.e., porosity, surface area, crystallinity, surface functionalities)¹⁹ of commercially available active carbons complicate systematic correlation of inherent carbon, transition metal, and nitrogen interactions and obscure the elucidation of their respective roles in the formation of catalytic materials. Furthermore, the difficulty in uniformly and reproducibly dispersing/mixing the transition metal and nitrogen precursors with activated carbons possessing poorly defined properties makes consistent and reproducible activity challenging to obtain.

Rather than dispersing active ORR catalysts on a preformed carbon support, an attractive alternative scheme is to produce the catalytic sites and carbon support simultaneously. Recently, we described the direct growth of carbon nanofibers (CNFs)

* Corresponding author. E-mail: stevenson@mail.cm.utexas.edu.

containing ~ 1 at. % N by pyrolysis of iron (II) phthalocyanine on nickel substrates.²⁰ In comparative studies with glassy carbon electrodes, the N-doped CNF electrodes demonstrated improved electrocatalytic activity for the ORR. We attributed the observed enhanced activity to the presence of edge plane defects and nitrogen functionalities within the CNF structure.²⁰ In the present work, nondoped and nitrogen-doped (N-doped) CNF electrodes were prepared via a floating catalyst chemical vapor deposition (CVD) method using precursors consisting of ferrocene and either xylene or pyridine to directly control the nitrogen content. This approach allows for the controlled growth and selective nitrogen doping of CNF electrodes and provides for a more direct basis for establishing correlations between carbon structure, texture, composition, and electrochemical activity. Specifically, we describe the direct preparation of N-doped CNF electrodes which exhibit enhanced catalytic activity over nondoped varieties. This methodology has enabled us to establish new insights as to the nature of the catalytic system and on the influence of nitrogen doping on the ORR at activated carbons. Mechanistic differences in the ORR reaction pathway between nondoped and N-doped CNF varieties are demonstrated and discussed.

Experimental Section

CNF Preparation. Nondoped and N-doped CNFs were produced through the floating catalyst CVD method,²¹ using a setup similar to that described by Rao et al.²² For studies conducted herein, an integrated, automated system consisting of programmable syringe pumps (New Era Pump Systems NE-1000), electronic gas mass flow controllers (MKS type 1179A), and two single-zone tube furnaces (Carbolite model HST 12/35/200/2416CG) interfaced through a single computer running a customized LabVIEW program was used. Argon (99.997%, Praxair) and hydrogen (99.95%, Praxair) were used as the purge and feed gases. Solutions consisting of 20 mg mL⁻¹ of ferrocene in xylenes (Fisher) or pyridine (EM Science) for growth of nondoped and N-doped CNFs, respectively, were loaded into 1.0 mL gastight glass syringes (Hamilton 81320). The syringes were interfaced with stainless steel lines that fed into the center of the front half of an airtight quartz tube (26 mm OD, 22 mm ID) located in furnace 1. The quartz tube spanned the two tube furnaces. Nickel (Alfa Aesar, 100 mesh gauze) electrode growth substrates were placed downstream approximately in the center of furnace 2. After a fifteen minute argon purge (200 sccm) of the quartz tube, furnace 2 was heated to the appropriate pyrolysis temperature (700/800 °C for nondoped and N-doped CNFs, respectively). Following a five minute thermal equilibration period, furnace 1 was heated to the vaporization temperature of the feed solution (150/130 °C for xylenes and pyridine, respectively). Concurrently, the reaction gas flow was started, amounting to a total gas flow of 575 sccm. 1 mL of the ferrocene solution was then fed into furnace 1 at a rate of 0.1 mL s⁻¹. Once completed, furnaces 1 and 2 were allowed to cool while the reaction gas flow was switched to 200 sccm argon for the remainder of the cooling process. Upon cooling to room temperature, CNFs were collected from the interior of the quartz tube in furnace 2 and/or the CNF-coated nickel mesh was removed. The resulting CNF films appeared as a uniform black felt-like layer. Collected materials were stored in individual airtight vials prior to analysis.

Structural Analysis. Transmission electron microscopy (TEM) of the resultant CNF materials was performed with a JEOL 2010F operating at 200 kV. Prior to analysis, the CNFs were dispersed in methanol and then dropped onto a Cu TEM

grid covered with a thin amorphous carbon film. Image analysis was performed with DigitalMicrograph 3.6.1 (Gatan) software. BET isotherm surface area measurements were obtained with a Micromeritics ASAP 2010. Samples were dried overnight in a vacuum at 200 °C, weighed, and then dosed with N₂ (molecular cross section = 0.1620 nm²) at -195.8 °C. Raman analysis was performed with a Renishaw In Via system utilizing 514.5 nm incident radiation. A 50 \times aperture (N.A. = 0.75) was used, resulting in approximately a 2 μ m diameter sampling cross section. Thermogravimetric analysis (TGA) of bulk CNF samples was conducted using a TA Instruments Q500 in Hi-Res Dynamic mode (heat rate = 50 °C min⁻¹, sensitivity = 1.00, resolution = 5.00). Sample sizes of 1 to 5 mg of CNFs were loaded into platinum pans and heated to 900 °C in a flowing air (Praxair, 99.998%) environment with a 60 mL min⁻¹ flow rate to the sample and a 40 mL min⁻¹ flow rate of N₂ (Praxair, 99.998%) to the balance. Residual mass after temperature ramp was shown by Raman spectroscopy to be hematite, Fe₂O₃. Therefore, the reported residual mass of the CNFs of the iron seed particle content is reported after correction for hematite oxygen content. X-ray photoelectron spectroscopy (XPS) was carried out with a PHI 5700 ESCA system utilizing Al K-alpha monochromatic (1486.6 eV) and calibrated using the signals for Au4f_{7/2}, Ag3d_{5/2}, and Cu2p_{3/2} at 83.98, 36.27, and 932.67 eV, respectively. The low iron sensitivity necessitated 10 scans averaged together to resolve the Fe 2p spectrum. The XPS spectra were peak fit and analyzed using a freeware software package, FITT 1.2 (Photoelectron Spectroscopy Lab, Seoul National University). The results of all reported analyses (TEM, Raman, TGA, XPS, chronocoulometry, and cyclic voltammetry) were verified by at least five replicate measurements made on different batches of CNFs. Therefore, all reported standard deviations represent true sample-to-sample variances calculated from at least five individual experiments.

Electrochemical Analysis. A single-compartment, three electrode, glass electrochemical cell was employed for the cyclic voltammetry and chronocoulometry studies. Platinum mesh (Aldrich) and Hg/Hg₂SO₄ (sat'd K₂SO₄, CH Instruments) were used as the counter and reference electrodes, respectively, while CNF-coated nickel mesh served as the working electrode. All electrode potentials are reported versus Hg/Hg₂SO₄ (sat'd K₂SO₄), which is ca. 0.64 V positive of NHE. All electrochemical measurements were taken with a quiescent solution. All electrochemical studies were conducted at room temperature (23 \pm 2 °C) and were performed with either a CH Instruments 700A potentiostat or an Autolab PGSTAT 30 interfaced to a PC. Geometric surface areas of the CNF electrodes were determined by chronocoulometry (CC) using hexaammineruthenium(III) chloride (Strem Chemicals) in 1 M KNO₃. The potential of the uncoated nickel mesh electrodes were stepped from -0.4 V to -0.8 V for 1 s and the area was calculated from the slope ($m = 2nFAD_o^{1/2}C\pi^{-1/2}$) of the linear portion of the Q vs $t^{1/2}$ plot using the diffusion coefficient²⁰ $D_o = 7.3 \times 10^{-6}$ cm² s⁻¹. For uncoated nickel mesh electrodes, the observed electroactive area was 1.1 ± 0.1 cm². The geometric surface areas of the CNF electrodes were assumed to be the same equivalent area as the uncoated nickel mesh electrodes.

For cyclic voltammetry and chronoamperometry studies, Ar or O₂ (99.5%, Praxair), introduced through a gas inlet of the electrochemical cell, was bubbled through the test solutions for 20 min prior to the start of the measurements (to either fully purge or to fully oxygenate, respectively) and again for one minute between measurements. Solution volumes were ~ 5 –7 mL. The cell was kept at ambient pressure. The diffusivity of

dissolved O_2 , assumed to be $1.75 \times 10^{-5} \text{ cm s}^{-1}$,²³ and the saturated oxygen concentrations, 1.0 mM and 1.3 mM in 1 M KOH and 1 M KNO_3 , respectively,²⁴ were used in calculations involving chronocoulometry. The solution was purged prior to and after each electrochemical experiment. Electrolyte solutions were prepared using potassium nitrate (EM Science, 99.9%) or potassium hydroxide (Aldrich, 99.99%) as received. The potassium nitrate and potassium hydroxide solutions were measured to have pH values of 6.7 and 14.0, respectively. Hydrogen peroxide solutions were made by diluting 30% H_2O_2 stock solutions (Fischer, with stabilizer). Cyclic voltammograms in the presence of O_2 were obtained by sweeping the potential from -0.2 V to -1.1 V at various sweep rates between 5 mV/s and 100 mV/s in corresponding supporting electrolytes. All CVs conducted in the presence of O_2 are background subtracted unless noted otherwise. Chronoamperometry studies for O_2 reduction were performed using a single potential-step method, stepping from an initial potential of -0.3 V to a final potential of -0.7 V or -1.1 V and recording the charge passed for a period of one second.

Determination of H_2O_2 Heterogeneous Decomposition Rate Constant. For 1 M KNO_3 solutions, a home-built manometer apparatus was employed. The manometer filled with O_2 saturated 1 M KNO_3 was attached to a 50 mL buret filled with O_2 saturated 1 M KNO_3 , similar to that described by Tseung et al.²⁵ A preweighed 1 to 10 mg sample of CNFs was dispersed in 50 mL. The nondoped CNF samples were noticeably more hydrophobic than the N-doped CNFs. Hence, to fully wet the nondoped CNFs a small aliquot ($<0.1 \text{ mL}$) of methanol was used. The wetted CNFs were immediately dispersed in solution, where the total methanol concentrations amounted to less than 5 mM. For N-doped CNF suspensions, measurements with and without added methanol showed no effect on peroxide decomposition within the precision of the measurements. The CNF suspensions were saturated with O_2 for 10 min while vigorously stirred with a magnetic stir bar. Following, 0.5 mL of 5 M H_2O_2 (standardized with $KMnO_4$ titration) was injected into the solution and the cell was immediately attached to the gasometric apparatus. The buret valve was opened periodically to level the manometer, unevened by the evolved $O_{2,g}$ from H_2O_2 decomposition. The volume of evolved $O_{2,g}$ was recorded every 30 to 60 s, for 20 to 60 min. All experiments were done with the single neck round-bottom cell immersed in a water bath set at $23.0 \pm 0.5^\circ \text{C}$. H_2O_2 concentrations were calculated as described by Carbonio et al.²⁶ For analysis in alkaline solutions, a preweighed 1 to 5 mg sample of CNFs was dispersed in 75 mL of 1 M KOH (99.99%, Aldrich) in a five neck cell including a gold rotating disk electrode (RDE) (PINE AFE2MO50AU), gas inlet/outlet, gold counter electrode, and reference electrode. The solution was purged with N_2 for 10 min while the gold RDE was rotated at 2000 rpm (PINE AFM SRX). Then, approximately 0.75 mL of 1 M H_2O_2 (30%, Aldrich, standardized with $KMnO_4$ (Aldrich) titration) was injected into the suspension while N_2 was blown over the solution. The gold RDE was swept from -0.7 V to -0.4 V at 50 mV/s to oxidize hydroperoxide at the electrode surface. Scans were recorded approximately every 60 s for 20 min. All experiments were done at room temperature ($23 \pm 2^\circ \text{C}$). In situ concentrations were calculated from the obtained limiting currents as described by Yeager et al.²⁷ First-order heterogeneous decomposition rate constants were determined from the linear slopes of $\ln[HO_2^-]$ vs time plots and solution volume and normalized by the CNF BET areas. BET analysis yielded areas of $130 \pm 10 \text{ m}^2 \text{ g}^{-1}$ for both nondoped and N-doped varieties.

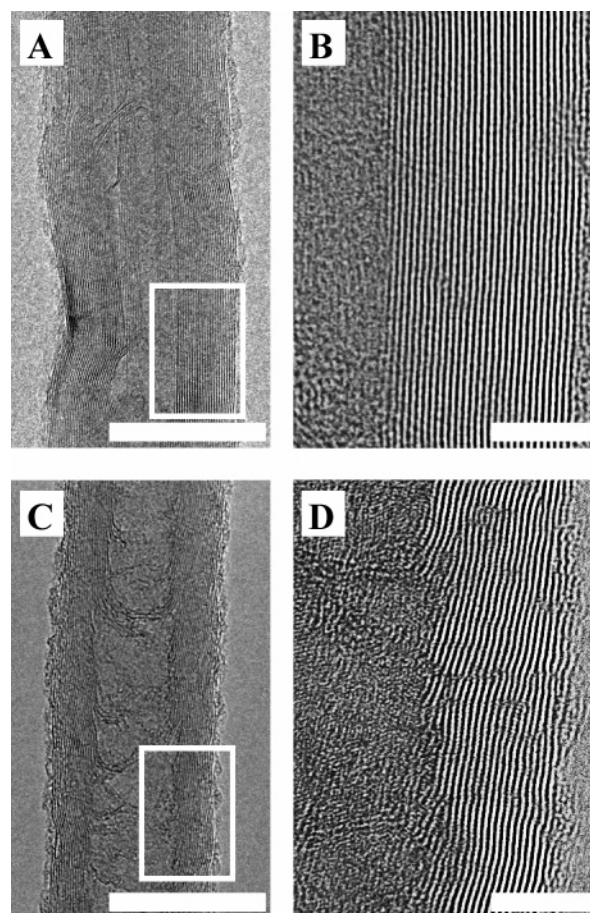


Figure 1. Representative TEM images of (A) nondoped, and (C) N-doped CNFs prepared by floating catalyst CVD. High-resolution TEM images (B) and (D) are of highlighted regions in (A) and (C), respectively. Scale bars: (A) and (C) are 20 nm, and (B) and (D) are 5 nm.

Results

Structural and Compositional Characterization. Figure 1 displays representative high-resolution TEM images of nondoped and N-doped CNF electrodes prepared by the floating catalyst CVD method. Both varieties of CNF electrodes exhibit similar fibril morphologies with 20–40 nm diameters, $>10 \mu\text{m}$ lengths, and hollow interiors for individual CNFs. Subtle structural differences are seen between the two CNF varieties, with N-doped CNF sidewall structures appearing more compartmentalized and disordered than nondoped analogues, consistent with other reports of carbon nanotubes grown under similar conditions.^{28,29} Additionally, the sidewalls of the N-doped CNFs contain more dislocations and disruptions in the graphene stacking (turbostratic disorder), in agreement with observations of Sjoström,³⁰ who noted that disruptions and irregular curvature in graphene stacking in N-doped carbons is due to the propensity of incorporated nitrogen to form pentagonal defects in the graphene sheets. The introduction of pentagons into the basal planes disrupts the planar hexagonal arrangement of C atoms found in graphite, causes buckling of the graphene layers, and results in interlayer distances that fluctuate between wider and thinner distances than found in pristine graphite. The average difference in interlayer spacings (d_{002}) between the two varieties can be estimated from the TEM images.³¹ Fourier transforms³² of Figures 1B and 1D yield d_{002} spacings of $3.448 \pm 0.005 \text{ \AA}$ and $3.53 \pm 0.02 \text{ \AA}$ for the nondoped and N-doped varieties, respectively, suggesting that N-doped CNFs are more turbostratic. Localized parallel electron energy loss

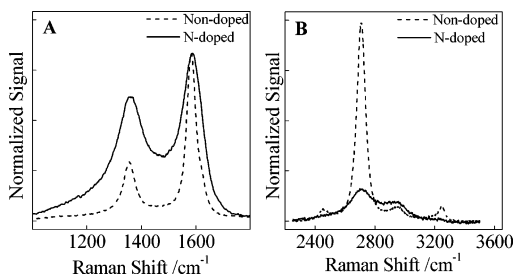


Figure 2. Representative Raman spectra of non-doped CNFs (dashed line) and N-doped CNFs (solid line). (A) First-order spectra and (B) second-order spectra are normalized to the intensity of the band at 1588 cm^{-1} .

spectroscopy (PEELS) experiments (data not shown) on the N-doped CNFs verified the presence of nitrogen at edge plane sites on the periphery of the fiber walls, consistent with that of Tang et al.³³ for similarly prepared materials. Low magnification electron micrographs of the structures in Figure 1 showed the presence of iron seed particles with diameters $<10\text{ nm}$ dispersed sporadically throughout CNF interiors and, much less frequently, on the exteriors. Visually, graphitic shells (carbon coatings) appear to surround all iron particles present on the CNF exterior. PEELS analysis of the encapsulated metallic particles demonstrated a strong iron signal. However, no iron signal was detectable when the beam was placed over areas without visible iron particles.

The differences in crystallinity of the two CNF types were assessed using Raman spectroscopy. Figure 2 displays representative first-order Raman spectra of the non-doped and N-doped CNFs. Both CNF types demonstrate strong bands near 1360 and 1590 cm^{-1} (Figure 2A), consistent with graphitic carbon samples.³⁴ The ratio of the intensities (I) of the two bands (D and G bands, respectively) can be used to estimate the extent of disorder within the samples.³⁵ Such analysis for our materials yields I_D/I_G ratios for the non-doped and N-doped CNF varieties of 0.36 ± 0.01 (1σ) and 0.74 ± 0.02 (1σ), respectively. The 2-fold increase in the I_D/I_G ratio for the N-doped material corresponds to a 2-fold decrease in the average in-plane crystalline domain size (L_c) of the wall structure and agrees with the TEM data presented above. In addition to the differences in I_D/I_G ratios, the spectra also exhibit a marked broadening of the full width at half-maximum (fwhm) of the D and G bands for the N-doped CNFs and a significant shoulder near $\sim 1250\text{ cm}^{-1}$. This is in agreement with the studies of Tascon et al.^{36,37} that indicate first order band broadening correlates strongly with the degree of graphitic disorder, noting a high energy shoulder of the D band is apparent with more disordered microcrystalline carbons. More surprising are the observed differences in the second-order Raman spectra.^{36,38} Figure 2B shows the second order Raman spectra for both CNF types, where the intensities have been normalized to the intensity of the G band in the first-order spectra (Figure 2A). Empirically, only well-resolved bands at $\sim 2700\text{ cm}^{-1}$ and $\sim 3250\text{ cm}^{-1}$ are observed for very crystalline graphitic carbons. For disordered carbons these bands are very weak or not seen.³⁸ For example, the intensity of the band at $\sim 2700\text{ cm}^{-1}$ (commonly referred to as the 2D band)³⁹ in Figure 2B is $1/8$ as intense for the N-doped CNFs than for the non-doped varieties. The band at 3250 cm^{-1} is not seen in the spectrum for N-doped CNFs. Both CNF types demonstrate a band near 2950 cm^{-1} . A small, broad band at $\sim 2950\text{ cm}^{-1}$ is not apparent in Raman spectra for basal plane highly oriented pyrolytic graphite (HOPG) or natural graphite, but is seen in spectra for edge-plane HOPG⁴⁰ and microcrystalline graphitic powders.^{36,38} Also of interest is the small band at $\sim 2450\text{ cm}^{-1}$

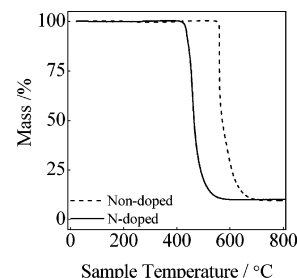


Figure 3. Representative TGA mass loss plots for non-doped CNFs (dashed line) and N-doped CNFs (solid line) conducted in air. The residual mass above $550\text{ }^{\circ}\text{C}$ is Fe_2O_3 (hematite) for both CNF varieties.

observed only for the non-doped materials. The origin of this mode is not clearly understood but has been noted in the spectra of basal plane graphite.⁴¹ We speculate that this band is associated with a larger abundance of basal plane sites or, conversely, a lack of edge plane sites. Hence, both the first and second-order Raman spectra suggest significant disorder in both CNF varieties, with a greater extent of disorder in the N-doped CNFs. For both CNF types, no discernible modes were visible below 1000 cm^{-1} (data not shown) to indicate the presence of single-walled carbon nanotubes. The absence of bands below 600 cm^{-1} also indicates that no iron oxides (e.g., magnetite, hematite, ferrihydrite, goethite) are present at detectable levels on the “as-grown” CNF electrodes.^{42,43}

TGA was conducted to assess thermal stabilities and residual iron catalyst concentrations in both CNF types. Figure 3 presents typical TGA curves for non-doped and N-doped CNFs. The maxima in first derivative plots of these curves were used to estimate burnoff temperatures of CNF materials in an oxidative environment.⁴⁴ Burnoff temperatures are functions of analysis conditions (e.g., analysis gas composition, flow rate, sample heating rate) and are thus potentially misleading if compared between dissimilar studies. However, comparisons of burnoff temperatures for samples analyzed under identical conditions can distinguish materials that are more easily thermally decomposed. For five measurements of each CNF type, burnoff temperatures for non-doped and N-doped CNFs were $540 \pm 40\text{ }^{\circ}\text{C}$ (1σ) and $450 \pm 10\text{ }^{\circ}\text{C}$ (1σ), respectively. The observed $\sim 90\text{ }^{\circ}\text{C}$ lower thermal decomposition temperature for the N-doped CNF electrodes supports the TEM and Raman data that these materials are more disordered and possess considerably more edge plane sites. These data are consistent with reports of Kinoshita et al.⁴⁵ which indicate that thermal decomposition temperatures for natural graphite powders decrease as the density of edge plane sites increase. For both CNF types, the remaining mass above $750\text{ }^{\circ}\text{C}$ was found to be hematite (Fe_2O_3).⁴³ The residual bulk iron mass percentages after oxygen content correction for non-doped and N-doped CNFs were 7 ± 1 (1σ) % and 9 ± 1 (1σ) %, respectively.

The elemental surface compositions of non-doped and N-doped CNF varieties were assessed using X-ray photoelectron spectroscopy (XPS). Figure 4 shows 10 scan-averaged Fe 2p spectra. The total surface iron content for the non-doped and N-doped CNFs is 1.2 and 1.1 at. %, respectively, which corresponds to $\sim 4.5\text{ wt } \%$ of the total amount of iron measured from TGA. The results of TGA are insensitive to the nature or position of the iron in the CNF samples and therefore report on the *total* residual iron content (i.e., all iron including that encapsulated by graphene layers which was by far the dominant form of iron species seen through TEM observations). Sampling depths of XPS and Raman under the experimental conditions are similar ($\sim 10\text{ nm}$)^{46,47} and thus the two techniques only report

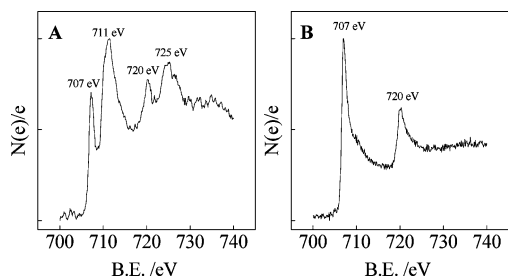


Figure 4. Normalized X-ray photoelectron Fe 2p spectra (10 scan average) for (A) nondoped CNFs, and (B) N-doped CNFs.

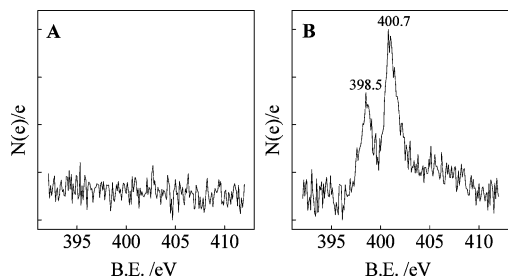


Figure 5. Normalized X-ray photoelectron N1s spectra (single scan) for (A) nondoped CNFs, and (B) N-doped CNFs.

on iron species within ~ 10 nm of the surface. Hence, because XPS analysis yields an iron content roughly half that of the total content determined by TGA, we estimate that half of the iron is encased by graphene layers no thinner than ~ 10 nm. Raman analysis seems less sensitive to iron content near or at the CNFs surface because only iron oxide species are Raman active. Further, since most iron oxide phases are only weakly Raman active, Raman analysis can only accurately reflect the iron species that are within ~ 10 nm of the CNF surface and that are iron oxides that are strong Raman scatterers, e.g., α - Fe_2O_3 .⁴³ Remarkably, the apparent oxidation state(s) of the iron in the two CNF varieties is different, with the N-doped CNFs exhibiting one pair of Fe $2p_{1/2}$ and $2p_{3/2}$ bands (707 and 720 eV) and the nondoped CNFs showing two pairs of bands (707 and 720 eV and 711 and 725 eV). The two sets of bands for nondoped CNFs are consistent with metallic (Fe^0) iron/iron carbide and iron oxides ($\text{Fe}^{2+/3+}$), respectively.^{48,49} In contrast, the surface iron content of the N-doped CNF materials appears to be solely metallic or iron carbide with the sharpness of the Fe bands strikingly similar to the standard Fe 2p spectrum for metallic iron,⁴⁹ suggesting that the iron is metallic rather than carbide. XPS peak areas indicate that the relative abundances of the metallic iron and iron oxides for nondoped CNFs is 45% and 55%, respectively. The broad nature of the 711 and 725 eV bands make it difficult to determine specifically which oxide form (e.g., hematite, ferrihydrite, etc.) is predominant in the nondoped CNFs.⁵⁰ Still, it seems clear that the surface iron of nondoped CNFs is of a mixed valent nature while that of the N-doped CNFs consists of zerovalent (metallic) iron. The oxidized iron is most likely due to exposure to atmospheric oxygen and reflects the differences in oxidative stability between nondoped and N-doped CNF varieties (vide infra). Figure 5 displays the N1s spectra for nondoped and N-doped CNFs. N-doped CNFs exhibit two strong bands at 398.5 and 400.7 eV and a weak, broad band at 405 eV, while nondoped varieties show no discernible N1s signal. The integrated signal intensity for nitrogen atoms for N-doped CNFs give a surface concentration of 4.0 at. %, consistent with that of Glerup⁵¹ for N-doped CNFs produced by a similar method. Several groups investigating nitrogen-doped graphitic carbons have proposed that the

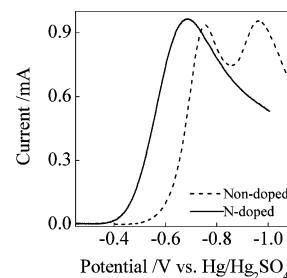


Figure 6. Background subtracted voltammetric responses of a non-doped CNF electrode (dashed line) and a N-doped CNF electrode (solid line) immersed in an O_2 saturated 1 M KNO_3 solution. Scan rate = 0.1 V s^{-1} .

bands at 398 and 401 eV correspond to “pyridinic” and “pyrrolic” nitrogen incorporation, respectively.^{52,53} The weak band near 405 eV may be attributable to nitrogen atoms substituted in the interior rather than periphery of the graphene sheets.⁵² Peak areas for the three visible N1s bands indicate that 31% of the incorporated nitrogen may be in the “pyridinic” form and that 59% of the nitrogen atoms may be present in the “pyrrolic” form. The remaining 10% of detectable nitrogen atoms represent quaternary-like nitrogens in the interior of the graphene sheets. For both CNF varieties the carbon is predominantly sp^2 hybridized as denoted by a C1s binding energy of 284 eV (data not shown), similar to that of HOPG.^{54,55} Additionally, no detectable sidebands in the C1s region (285–291 eV) are present to suggest the existence of graphene oxides or oxygen containing functionalities on the CNF electrodes.⁵⁶ A small O1s signal at 532.6 eV (data not shown) is also seen for both CNF varieties consistent with the presence of adsorbed molecular oxygen or H_2O .

Reduction of Oxygen. In a previous report, we noted that N-doped CNF electrodes prepared from the pyrolysis of iron(II) phthalocyanine were active electrocatalysts for the ORR in comparison to glassy carbon electrodes.²⁰ In an effort to more directly compare the influence of nitrogen doping we prepared both nondoped and N-doped CNF electrodes using precursors consisting of ferrocene and either xylene or pyridine. As detailed above, this approach has allowed us to control carefully the nitrogen surface content while maintaining consistent iron loadings and morphological properties (i.e., fibril diameters and lengths). Further, through this synthetic route we have been able to grow CNFs directly on current collector supports, enabling us to study the electrochemical behavior of the CNFs without potentially biasing the behavior due to incorporation of extraneous materials (e.g., binders) and procedural steps (e.g., suspending CNFs in solution with surfactants and then casting the suspension on a separate electrode surface). The background-corrected voltammetric responses for the ORR at nondoped and N-doped CNF electrodes in an O_2 saturated 1 M KNO_3 solution ($\text{pH} = 6.4$) are shown in Figure 6. Marked differences between the two CNF variants can be easily seen. In particular, only a single reduction peak at $E_{p1} = -0.69 \text{ V}$ (vs $\text{Hg}/\text{Hg}_2\text{SO}_4$) for the ORR is observed for N-doped CNF electrodes, whereas two reductive peaks at $E_{p1} = -0.76 \text{ V}$ and $E_{p2} = -0.97 \text{ V}$ are seen for nondoped CNF electrodes. Additionally, for N-doped CNFs the ORR peak is shifted significantly positively (ca. 70 mV) relative to the response for nondoped CNF. This positive potential shift implies that the N-doped CNF electrodes are more catalytically active (kinetically more facile) for O_2 reduction. Figure 7 displays voltammetric responses for the reduction of O_2 in more basic 1 M KOH oxygen saturated solutions. In alkaline conditions, $\text{pH} > 10$, the voltammograms for nondoped and N-doped CNFs are very similar, each with two well-

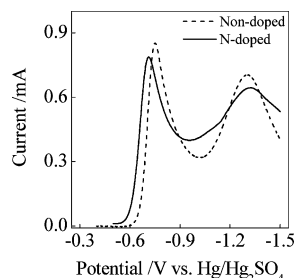


Figure 7. Background subtracted voltammetric responses of a non-doped CNF electrode (dashed line) and a N-doped CNF electrode (solid line) immersed in an O_2 saturated 1 M KOH solution. Scan rate = 0.1 V s^{-1} .

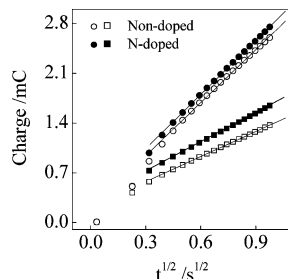
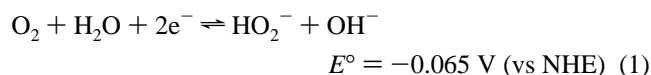


Figure 8. Chronocoulometric response of non-doped CNF (open symbols) and N-doped CNF (dark symbols) electrodes immersed in O_2 saturated 1 M KNO_3 and 1 M KOH. The electrodes were stepped from -0.30 V to -1.10 V in 1 M KNO_3 (\circ, \bullet) and from -0.40 V vs to -1.0 V in 1 M KOH (\square, \blacksquare).

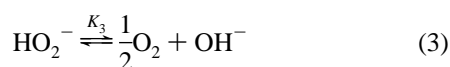
separated peaks, with the first peak at $\sim E_{p1} = -0.71 \text{ V}$ for the N-doped CNFs and at $E_{p1} = -0.75 \text{ V}$ for the non-doped CNFs. In general, the electrochemical response for O_2 reduction is consistent with the well-described behavior at unmodified graphitic carbon electrodes in neutral to alkaline media. Under these conditions the ORR proceeds by a two-electron reduction pathway, eq 1, with hydrogen peroxide (HO_2^- , hydroperoxide in neutral to alkaline media) as an intermediate or final product.



This reaction may be followed either by a second two-electron reduction of HO_2^- to OH^- , eq 2,



or, by the rapid chemical decomposition of HO_2^- to regenerate O_2 , eq 3.

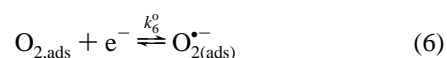


Whether the hydroperoxide species undergoes further electrochemical reduction (eq 2) or decomposes (eq 3), the whole ORR process starting with the “two-electron pathway” involves four electrons per oxygen molecule. For our CNF electrodes, quantitative assessment of the number of electrons, n , involved in O_2 reduction was performed using chronocoulometry. Determination of n is possible from the slopes of the chronocoulometric plots shown in Figure 8, using eq 4,⁵⁷ where Q is the measured charge, F is Faraday’s constant, A is the geometric area of the electrode, D_{O_2} is the diffusion coefficient of dissolved O_2 , C_{O_2} is the concentration of dissolved oxygen, and t is time.

$$Q = 2nFAD_{O_2}^{1/2}C_{O_2}\pi^{-1/2}t^{1/2} \quad (4)$$

Nondoped and N-doped CNF electrodes in 1 M KNO_3 give similar values of 3.7 ± 0.4 and 3.6 ± 0.4 electrons at -1.10 V , respectively, indicating that the electrochemical process of the broad single wave for N-doped CNFs is identical to the sum process of the sharp two waves for nondoped CNFs, where one equivalent of O_2 undergoes a net four electron reduction at -1.10 V for both CNF types. For conventional graphitic electrodes in the absence of additional catalysts (e.g., Pt),^{2,3} both successive two electron reductions of O_2 (eq 1 and 2) are observed since the slow kinetics of the chemical decomposition step (eq 3) make hydroperoxide a stable intermediate.

Although exhaustive mechanistic analysis of the ORR is difficult given the numerous possible pathways, linear sweep voltammetry can provide insight on the rate determining step (RDS) and whether an outer sphere (nonadsorptive) or inner sphere (adsorptive) pathway is observed.⁵⁸ Many investigators, including Mrha,⁸ Yeager², and McCreery⁵⁹ have proposed that, at metal-free carbon surfaces, O_2 reduction involves surface adsorption (eq 5), with the initial electron-transfer step consisting of O_2 being reduced to superoxide (eq 6), followed by protonation to form hydroperoxide radical (eq 7) and subsequent reduction to hydroperoxide (eq 8).



McCreery et al.⁵⁸ have argued that since the pK_A of the superoxide species likely shifts from ~ 4 to ~ 9 when it is adsorbed rather than when it is free in solution, the protonation step (eq 7) at all pH values less than the pK_{A,O_2^-} should be fast. Hence, for O_2 reduction in solutions with the $pH < pK_{A,O_2^-}$, the RDS is the initial electron-transfer rather than the protonation of $O_{2(ads)}^{\bullet-}$.⁵⁸ Technically, the RDS should shift from eq 6 to eq 7 for O_2 reduction proceeding via the adsorptive pathway, yielding a value of $\alpha_{obs} = 0.5$ at neutral pH and increasing to a value near $\alpha_{obs} = 1$ in very alkaline conditions. From the voltammetry shown in Figures 6 and 7, α_{obs} can be estimated from the measured width of the waves ($E_{p/2} - E_p = 1.875RT/\alpha_{obs}F$), where E_p is the potential where the peak current is observed and $E_{p/2}$ is the potential at exactly one-half the total peak current.⁶⁰ For N-doped CNF electrodes at $pH = 6.7$, $\alpha_{obs} = 0.4$; whereas for nondoped varieties, $\alpha_{obs} = 0.8$. In $pH = 14$ solutions, the values for α_{obs} were 0.8 and 1.0 for N-doped and nondoped CNFs, respectively. The N-doped CNFs exhibit a change in charge-transfer coefficient, α_{obs} , consistent with a strongly adsorptive pathway while the nondoped CNFs show voltammetry and a respective α_{obs} that is invariant to solution pH, suggesting that O_2 is not strongly adsorbed at the nondoped CNFs in the studied pH range.

While the α_{obs} dependences reflect differences in the non-adsorptive and adsorptive pathways for the nondoped and N-doped CNFs, respectively, the dissimilarities in voltammetric features also indicate that the ORR mechanistic steps are different, especially in $pH < 10$ solutions. In particular, the positive shift in the O_2 reduction wave is suggestive of an

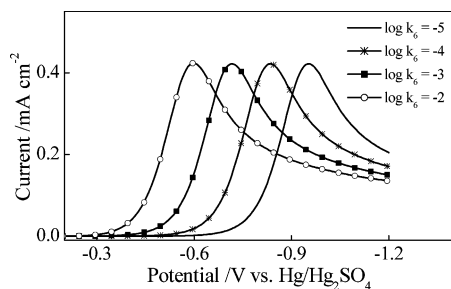


Figure 9. Simulated oxygen reduction voltammograms with varied values for the first electron-transfer step (Reaction 3) rate constant, k_6^o . Scan rate = 0.1 V s^{-1} .

adsorptive pathway⁵⁹ and consistent with the idea that the electron-transfer rate for reduction of O_2 to $\text{O}_2^{\bullet-}$ (eq 6) is accelerated when adsorbed. To better assess this behavior, a commercial simulations package was used to model the observed voltammetry. The appendix describes the parameters used for the simulation in more detail. Figure 9 shows the effect of the rate constant⁶¹ on the O_2 reduction potential associated with the first electron-transfer step (O_2 to $\text{O}_2^{\bullet-}$, k_6^o , eq 6). Variations in the value of k_6^o over a small range of orders of magnitude shift $E_{p/2}$ of the first reduction peak by several hundred millivolts, indicating a strong sensitivity of the position of the oxygen reduction peak toward the rate of the initial electron-transfer step. The 125 mV difference in $E_{p/2}$ between the voltammograms in Figure 6 reflects a 10-fold increase in k_6^o . This is consistent with the idea that O_2 reduction to $\text{O}_2^{\bullet-}$ with $\text{pH} < 10$ is limited by the first electron-transfer step (eq 6) rather than the proton-transfer step (eq 7). In contrast, the difference in $E_{p/2}$ observed for the reduction of oxygen to hydroperoxide in more alkaline solutions ($\text{pH} > 10$) between the CNF varieties (see Figure 7) is only 48 mV. Since α_{obs} values for both CNF types are near 1 and chronocoulometric analysis (Figure 8) yields $n = 2$ (two-electrons) for the first peak for both CNF varieties, the reduction of O_2 to $\text{O}_2^{\bullet-}$ is likely mechanistically similar for N-doped and nondoped CNFs in alkaline conditions. The slight peak shift between N-doped and nondoped CNFs in Figure 7 is most likely a result of the larger edge plane graphite content in N-doped CNFs observed in the Raman, TGA, and TEM analyses, as demonstrated by McCreery et al.⁵⁹

The lack of a second voltammetric peak for N-doped CNF electrodes in solutions of neutral pH (Figure 6) suggests an additional difference in the reaction pathway for O_2 reduction where the intermediate, hydroperoxide (HO_2^-), is much less stable at the CNF/solution interface. We also simulated the influence of the rate of the observed heterogeneous hydroperoxide decomposition (eq 3) on O_2 reduction voltammetry.^{62–64} McIntyre has previously reported similar modeling studies of the ORR.^{62,65} Following this precedent, we simulated the two successive, two electron-transfer O_2 reduction pathways and modeled a heterogeneous chemical regeneration step for the recycling of O_2 (see appendix for simulation parameters). Figure 10 shows the influence of forward rate constant for the heterogeneous chemical decomposition of hydroperoxide, $k_{3,f}$, (eq 3) varied over 6 orders of magnitude. With small $k_{3,f}$ values ($< 10^{-4} \text{ cm s}^{-1}$), oxygen regeneration (recycling) is negligible and two separate reduction peaks are observed. With larger values of $k_{3,f}$ ($> 10^{-3} \text{ cm s}^{-1}$), a transition from two observed peaks to only one observed peak is seen. The absence of the second reduction peak suggests that electrochemically generated hydroperoxide chemically decomposes to oxygen at a rate faster than the rate at which it is electrochemically reduced to OH^- .

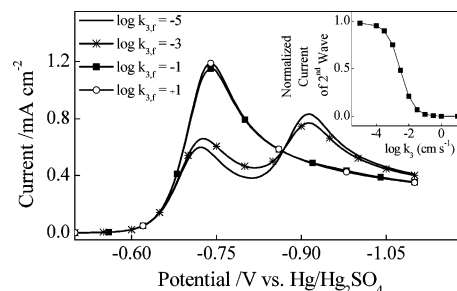


Figure 10. Simulated voltammograms of the peroxide pathway reduction of oxygen with varied values for the heterogeneous hydroperoxide decomposition rate constant, $k_{3,f}$. The effect of $k_{3,f}$ on the normalized hydroperoxide reduction currents is shown in the inset. Scan rate = 0.1 V s^{-1} .

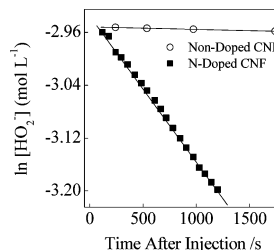


Figure 11. Gasometric analysis of the heterogeneous decomposition of hydroperoxide at nondoped CNFs (O) and N-doped CNFs (■) in 1 M KNO_3 .

A key feature of this simulation is that the transition between the two extreme conditions occurs within a small range encompassing 3 orders of magnitude of $k_{3,f}$, as indicated in the inset of Figure 10.

To assess experimentally whether the chemical decomposition rates of hydroperoxide were in fact different between the two CNFs varieties, we performed rotating disk electrode analyses in alkaline solutions;²⁷ but, because of difficulties in electrochemical detection of hydroperoxide in solutions of neutral pH,⁶⁶ gasometric analyses⁶⁷ were conducted in 1 M KNO_3 . Figure 11 shows representative results for the measured hydroperoxide decomposition rates at N-doped and nondoped CNFs. For N-doped CNFs, $k_{3,f}$ was found to be $5.1 \pm 0.7 \times 10^{-6} \text{ cm s}^{-1}$ and for nondoped CNFs, $k_{3,f}$ was $3.0 \pm 0.4 \times 10^{-8} \text{ cm s}^{-1}$. In 1 M KOH , the $k_{3,f}$ values for N-doped and nondoped CNFs were measured by RDE analysis to be $1.8 \pm 0.5 \times 10^{-5} \text{ cm s}^{-1}$ and $1.0 \pm 0.4 \times 10^{-7} \text{ cm s}^{-1}$, respectively. In both neutral and alkaline pHs, the N-doped CNFs demonstrate over a 100-fold increase in catalytic activity. Surprisingly, these values are within an order of magnitude of decomposition rates reported for most active catalysts, e.g., Pt-black.⁶⁸ Our observations are also in agreement with studies of other nitrogenated carbons showing similar hydroperoxide decomposition activity.¹¹ The slight increase of $k_{3,f}$ in alkaline solutions has been reported for other peroxide decomposition catalysts and is most likely attributable to a greater instability of hydroperoxide with increasing pH alkaline solutions.²⁵ Irrespective of the solution pH, the heterogeneous decomposition of hydroperoxide appeared to be first order (cm s^{-1}) at both CNF types, in agreement with reported first-order behaviors of other graphitic carbons and most metal oxide based catalysts.⁶⁴

One question that remains is why the hydroperoxide decomposition rate constant, $k_{3,f}$ (eq 3), values measured for the N-doped CNFs in neutral and alkaline pH media are 3 orders of magnitude smaller than those values predicted by our electrochemical simulations. This discrepancy may be rationalized by the limitations of the model and simplified simulation

parameters, i.e., the exclusion of the influence of reactant adsorption and decomposition reaction intermediates. The simulation presented here follows McIntyre's approach⁶² and treats the hydroperoxide decomposition in one uncomplicated chemical step that is confined to the surface but with no reactants as adsorbed species. As discussed by Appleby,⁶⁹ the actual catalytic regeneration of oxygen from hydroperoxide likely involves numerous adsorbed reactive intermediates such as $\text{O}_2^{\bullet-}$, HO_2^{\bullet} , and HO^{\bullet} . The absence of such intermediates in the decomposition step oversimplifies the potential dependence of the hydroperoxide decomposition reaction as the aforementioned intermediates are all likely reduced at the potentials necessary for oxygen reduction. Further, the relevant rate limiting step for the simulation may not be the same as for the gasometric or RDE bulk measurements conducted at open circuit conditions. The observance of a first order rate behavior in the experimental data suggests that the rate limiting step in reactions measured by bulk measurements is unimolecular, possibly involving an initial adsorption of hydroperoxide. Subsequent bimolecular surface bound reactions, as in the homogeneous case,⁷⁰ are likely rapid. Hence, if the hydroperoxide species is already adsorbed, as is the case in the in-situ generation of hydroperoxide during the ORR, the decomposition of the hydroperoxide species is not limited by adsorption but instead proceeds at the rate of the slowest subsequent step, which is likely to be several orders of magnitude faster than an initial adsorption step(s). This may also explain the observance of the second peak in the O_2 reduction voltammetry for N-doped CNFs in strongly alkaline solutions. Although RDE measurements show the $k_{3,f}$ value for N-doped CNFs remains 2 orders of magnitude greater than the value for nondoped CNFs in 1 M KOH, the second peak corresponding to the electrochemical reduction of hydroperoxide to OH^- is not suppressed. Alkaline solutions may favor an initial adsorptive step for hydroperoxide, as suggested by the RDE measurements. However, the greater stability of intermediates such as $\text{O}_2^{\bullet-}$, HO_2^{\bullet} , and HO^{\bullet} in alkaline solutions could impede subsequent steps in the disproportionation relative to the rates observed in 1 M KNO_3 . If the decomposition steps of the hydroperoxide species have slowed by only 2 orders of magnitude, the electrochemical reduction of hydroperoxide should be observed. While the specific cause for the reappearance of the peroxide reduction peak in more alkaline solutions at N-doped CNFs is unclear, the dissimilarity of the voltammograms of Figure 6 and the similarity in Figure 7 strongly indicate that the mechanism for oxygen adsorption and hydroperoxide decomposition at N-doped CNFs is strongly dependent on pH.

We feel that the activity of the N-doped CNFs toward oxygen reduction and hydroperoxide decomposition is a direct result of nitrogen doping and is not directly related to the residual iron content. While many have speculated that iron species may participate in the observed catalytic activity in as many as three ways (as exposed solid iron on the carbon surface, as dissolved iron species leaching out of the CNFs into solution, or as nitrogen-chelated $\text{Fe}^{2+}/\text{Fe}^{3+}$ sites), we have found no evidence to support any of these scenarios for our materials. In particular, we observe no voltammetric peaks commensurate with the oxidation of metallic iron or reduction of iron oxide on the surface of the CNFs. This is consistent with our TEM observations that all iron particles are encased by at least 2–3 graphene layers. Moreover, since TGA and XPS results demonstrate nominally equivalent loadings of iron for both CNF types, it seems unlikely that solid-phase surface iron species could be catalytically active for only the N-doped CNFs and not the

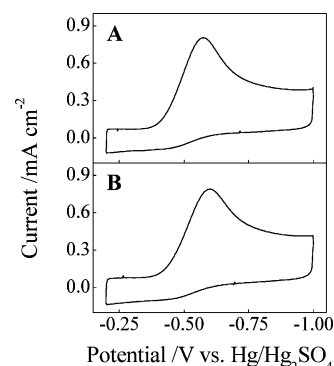


Figure 12. Uncorrected voltammetric response of a N-doped CNF electrode immersed in an O_2 -saturated 1 M KNO_3 solution (A) before and (B) after saturating the solution with CO. Scan rate 0.05 V s^{-1} .

undoped varieties. Tseung et al.⁷¹ hypothesized that dissolved transition metal hydroxides leached from metal surfaces can act as aqueous, Fenton-like peroxide decomposition catalysts (i.e., $\text{Fe}^{2+}/\text{Fe}^{3+}$ redox mediated peroxide decomposition). We see no evidence for iron species leaching into solution. In preliminary experiments⁷² we have quantified iron leaching rates from suspended CNF materials in solutions with neutral to alkaline pH. These leaching rates are extremely slow (<10 femtomoles $\text{L}^{-1} \text{ s}^{-1}$) so it seems highly unlikely that a Fenton-like catalyzed decomposition mechanism is operative. Additionally, we see no evidence for the presence of iron-chelated surface sites (i.e., FeN_2/C or FeN_4/C) that could act as Fenton-type catalysts and/or as facile O_2 adsorption sites as proposed by Dodelet¹⁶ and Schulenburg.⁷³ If this were the case then these sites should be easily poisoned in the presence of CO due to strong irreversible binding to the active iron site. As demonstrated in Figure 12, the O_2 reduction voltammetry at N-doped CNFs is unaffected, i.e., the peak shape, position, and absence of a second reductive peak, even when the solution has been saturated with CO ($\sim 1 \text{ mM}$). If nitrogen-chelated $\text{Fe}^{2+}/\text{Fe}^{3+}$ sites were influential, then exposure to CO should also inhibit hydroperoxide decomposition and result in observable changes in the O_2 reduction voltammetry.

As our electrochemical simulations qualitatively demonstrate, we believe that the increased catalytic activity and more positive O_2 reduction potential observed for N-doped CNF electrodes is predominantly a result of enhanced adsorption which proceeds to accelerate O_2 reduction and to advance heterogeneous hydroperoxide decomposition. This idea supports the original position of Yeager² and Wiesener^{74,75} that the transition metal (iron in this case) serves primarily to facilitate the stable incorporation of nitrogen into the graphitic structure during the CNF growth. This hypothesis is consistent with the ability of iron to alloy with carbon and nitrogen,²⁸ where at elevated temperatures the supersaturation of iron particles is relieved by the precipitation of both carbon and nitrogen, as detailed by Baker et al.⁷⁶ Hence, iron acts as a secondary participant in the formation of active carbon, i.e., as an agent to stabilize the incorporation of nitrogen within the graphene matrix. Increased nitrogen doping has repeatedly been noted to increase the basic nature^{11,56,77} and catalytic activity^{11,78,79} of the graphitic carbon. As indicated by Radovic et al., the enhanced basicity of the carbons is a consequence of strong π electron delocalization.⁸⁰ Delocalized π electrons are capable of nucleophilic attack, imparting to the carbon a Lewis basicity independent of basic heteroatom functionalities. The basic nature imparted on the N-doped CNFs likely stems from both the existence of electron-rich nitrogen sites (e.g., pyridinic nitrogen possesses one lone

pair of electrons in addition to the one electron donated to the conjugated π bond system) and from the stability against oxidation of the carbon which generally forms acidic oxygen functionalities. This is in accord with pH_{pzc} measurements (the pH where the net surface charge is zero) by Biniak et al.¹¹ of nitrogenated carbons and our own preliminary pH_{pzc} observations⁷² of N-doped CNFs that exhibit a basic nature ($\text{pH}_{\text{pzc}} \sim 9$).

The importance of the basic nature of N-doped CNFs is supported by earlier conclusions of Marsh et al.⁸¹ which indicate that nitrogen incorporation produces activated carbons with increased stability toward oxidation. This nitrogen-induced stability is also reflected in the difference in the Fe 2p XPS data (Figure 5) between our CNF varieties. The observance of only metallic (zerovalent) iron in N-doped CNFs suggests that these carbons have a more reducing nature that prevents oxidation. As suggested by Strelko et al.⁸² the strong Lewis basicity of N-doped carbons acts to facilitate reductive O_2 adsorption at open circuit conditions without the irreversible formation of oxygen functionalities. This has been experimentally verified by Boehm et al.⁵³ through observations of adsorbed $\text{O}_2^{\bullet -}$ on ammonia-treated carbons that showed enhanced catalytic activity for oxidative reactions (i.e., NO_2 , SO_2). We propose a similar prevalence of adsorbed $\text{O}_2^{\bullet -}$ on the surface of the N-doped CNFs which serves as the active species for driving the heterogeneous decomposition of hydroperoxide. Adsorbed $\text{O}_2^{\bullet -}$ likely reacts with hydroperoxide⁵³ to form more reactive species (e.g., HO_2^{\bullet} and HO^{\bullet}) that proceed to decompose hydroperoxide via surface analogues of chemical steps described by Bielski.⁷⁰ Biniak et al. have noted a decreased oxygen reduction overpotential for nitrogenated carbons that demonstrate faster rates of hydrogen peroxide decomposition.¹¹ We have also noted a strong correlation between the oxygen reduction peak potential and the nitrogen dopant level, where the oxygen reduction peak potential for a given scan rate shifts $\sim +30$ mV per 1% at N incorporated.⁸³ In light of the presented evidence, the strong adsorptive nature of the N-doped CNFs drives the more facile oxygen reduction observed at neutral pH. At more alkaline pH, it is unclear what determines the shift of N-doped CNF electrodes to O_2 reduction behavior similar to that observed at nondoped CNFs. Likely, the specific interplay of the ORR intermediates determines the fate of in situ generated hydroperoxide. Future experiments are planned to determine the specific intermediates and reactions responsible for controlling the decomposition of in situ generated hydroperoxide.

Summary

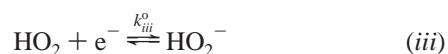
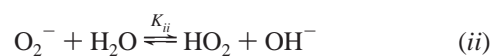
The structural, textural, and compositional features of N-doped and nondoped CNFs prepared by floating catalyst CVD were reported. Electrochemical studies of oxygen reduction of these materials demonstrated marked differences in catalytic activity. Experimental results and electrochemical simulations of “as-grown” N-doped CNF electrodes demonstrate that the incorporation of nitrogen into the carbon nanofibers results in more facile adsorption of oxygen and the greater activity for heterogeneous hydroperoxide decomposition. A mechanism is proposed where at N-doped CNF electrodes the reduction of O_2 in $\text{pH} < 10$ solutions proceeds by a two-electron process with the rate-limiting step controlled by adsorbed superoxide. In $\text{pH} > 10$ solutions, the adsorption process is hindered at the N-doped CNFs and is limited by rate of protonation of superoxide. Digital simulations of the observed voltammetry support the proposed mechanism for N-doped CNFs for the existence of accelerated kinetics of both the initial reduction of O_2 to $\text{O}_2^{\bullet -}$ and for the heterogeneous decomposition of hydrogen peroxide. The prepa-

ration of N-doped CNFs directly on conductive supports with tuned chemical and structural properties may prove useful for implementation in advanced sensors, batteries, and fuel cells.

Acknowledgment. Financial support of this work was provided in part by the R. A. Welch Foundation (Grant F-1529) and NSF. S.M. acknowledges the Harrington Foundation and the NSF for fellowship support. The authors thank Dr. Stephen Feldberg for informative discussions on the use of Digisim. S.M. also thanks Mr. Ryan Williams for assistance with LabVIEW programming and the Sessler group for help with organic solvent preparation.

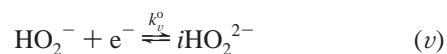
Appendix

Electrochemical Simulations. Digisim 3.05 (Bioanalytical Systems) was used to simulate both the effect of variation of the rate constants for the first electron-transfer step and the catalytic decomposition of hydrogen peroxide on O_2 reduction voltammetry. The following reaction scheme was entered into Digisim. General simulation parameters were $\nu = 0.1 \text{ V s}^{-1}$, $C_{\text{O}_2} = 1 \text{ mM}$, $D = 1 \times 10^{-5} \text{ cm}^2 \text{ s}^{-1}$ (for all species). The pH was set to 7.



Steps *i* and *iii* were set with the following conditions: E_i^0 and E_{iii}^0 were -0.6 and 1.0 V , respectively. α for both steps was 0.5 . The electron-transfer rate constant for step *iii* (k_{iii}^0) was $1 \times 10^6 \text{ cm}^2 \text{ s}^{-1}$. Assuming superoxide in step *ii* is adsorbed with a $\text{p}K_A \sim 9$,⁵⁸ the equilibrium constant for step *ii* was set to 1×10^{-5} ($\text{p}K_w - \text{p}K_A$) with a rapid forward rate constant ($k_{ii,f} = 1 \times 10^3$).

The catalytic regeneration of oxygen from hydroperoxide was simulated as a heterogeneous chemical reaction with a simplified ORR scheme.



Reactions *iv* and *viii* were set with the following conditions: $E_{iv}^0 = -0.3 \text{ V}$, $\alpha = 0.5$, $k_{iv}^0 = 1 \times 10^{-9} \text{ cm}^2 \text{ s}^{-1}$, and $E_{viii}^0 = 0.75 \text{ V}$, $\alpha = 0.5$, and $k_{viii}^0 = 1 \times 10^{-30} \text{ cm}^2 \text{ s}^{-1}$, respectively. The net sum of reactions *v*–*vii* is the chemical decomposition of hydroperoxide, but separating the chemical reaction into faux electron-transfer half reactions pinned the regeneration of oxygen at the electrode surface rather than the bulk solution. By setting $\alpha = 0$ for step *v* and the rates fast for steps *vi* and *vii*, k_{vi}^0 for step *v* exhibits no potential dependence and

becomes equivalent to the first-order heterogeneous decomposition rate constant, k_{3f} , with units of cm s^{-1} . Parameters for steps *vi* and *vii* were $E_v^0 = -2 \text{ V}$, $\alpha = 0.5$, $k_v^0 = 1 \times 10^3$, and $K_{vii} = 1 \times 10^{12}$, $k_{vii,f} = 1 \times 10^{12} \text{ M}^{-1} \text{ s}^{-1}$, respectively.

References and Notes

- Rodriguez-Reinoso, F. *Carbon* **1998**, *36*, 159.
- Yeager, E. *Electrochim. Acta* **1984**, *29*, 1527.
- Kinoshita, K. *Carbon: Electrochemical and Physicochemical Properties*; John Wiley and Sons: New York, 1988; pp 360–372.
- Savadogo, O. "The concept of synergetic materials in the electrocatalysis of the oxygen reduction reaction (ORR) in fuel cells"; New Materials for Fuel Cell Systems I, Proceedings of the International Symposium on New Materials for Fuel Cell Systems, 1st, Montreal, July 9–13, 1995, pp 544–576.
- Yeager, E. *J. Mol. Catal.* **1986**, *38*, 5.
- Chen, C. Y.; Yang, P. J. *Power Sources* **2003**, *123*, 37.
- Vinke, P.; van der Eijk, M.; Verbree, M.; Voskamp, A. F.; van Bekkum, H. *Carbon* **1994**, *32*, 675.
- Mrha, J. *Collect. Czech. Chem. Commun.* **1967**, *32*, 708.
- Lahaye, J.; Nanse, G.; Bagreev, A.; Strelko, V. *Carbon* **1999**, *37*, 585.
- Boehm, H. P.; De Rincon, A. R.; Stoeck, T.; Tereczki, B.; Vass, A. *J. Chim. Phys. Phys.-Chim. Biol.* **1987**, *84*, 1449.
- Biniak, S.; Walczyk, M.; Szymanski, G. S. *Fuel Process. Technol.* **2002**, *79*, 251.
- Jasinski, R. J. *Electrochem. Soc.* **1965**, *112*, 526.
- Vanveen, J. A. R.; Visser, C. *Electrochim. Acta* **1979**, *24*, 921.
- Janke, H. S., M.; Zimmerman, G. *Chem. Forsch.* **1986**, *61*, 133.
- Scherson, D.; Tanaka, A. A.; Gupta, S. L.; Tryk, D.; Fierro, C.; Holze, R.; Yeager, E. B.; Lattimer, R. P. *Electrochim. Acta* **1986**, *31*, 1247.
- Lefevre, M.; Dodelet, J. P. *Electrochim. Acta* **2003**, *48*, 2749.
- Lalande, G.; Cote, R.; Guay, D.; Dodelet, J. P.; Weng, L. T.; Bertrand, P. *Electrochim. Acta* **1997**, *42*, 1379.
- Wei, G.; Wainright, J. S.; Savinell, R. F. *J. New Mater. Elect. Syst.* **2000**, *3*, 121.
- Kinoshita, K. *Carbon: Electrochemical and Physicochemical Properties*; John Wiley and Sons: New York, 1988; pp 1–19.
- Maldonado, S.; Stevenson, K. J. *J. Phys. Chem. B* **2004**, *108*, 11375.
- Endo, M. *Chemtech.* **1988**, *18*, 568.
- Andrews, R.; Jacques, D.; Rao, A. M.; Derbyshire, F.; Qian, D.; Fan, X.; Dickey, E. C.; Chen, J. *Chem. Phys. Lett.* **1999**, *303*, 467.
- Electrochemical Oxygen Technology*; Kinoshita, K., Ed.; John Wiley and Sons: New York, 1992; p 9.
- Oxygen solubility in 1 M KNO_3 was estimated using i_L for a Au UME ($r = 12.5 \mu\text{m}$) relative to the corresponding i_L in 1 M KOH.
- Goldstein, J. R.; Tseung, A. C. C. *J. Catal.* **1974**, *32*, 452.
- Falcon, H.; Carbonio, R. E. *J. Electroanal. Chem.* **1992**, *339*, 69.
- Carbonio, R. E.; Tryk, D.; Yeager, E. B. "The use of electrochemical and non-electrochemical methods for the determination of peroxide decomposition rate constants"; Proceedings – Electrochemical Society, 1987, 87–12, pp 238–255.
- Trasobares, S.; Stephan, O.; Colliex, C.; Hsu, W. K.; Kroto, H. W.; Walton, D. R. M. *J. Chem. Phys.* **2002**, *116*, 8966.
- Terrones, M.; Ajayan, P. M.; Banhart, F.; Blase, X.; Carroll, D. L.; Charlier, J. C.; Czerw, R.; Foley, B.; Grobert, N.; Kamalakara, R.; Kohler-Redlich, P.; Ruhle, M.; Seeger, T.; Terrones, H. *Appl. Phys. A* **2002**, *74*, 355.
- Sjostrom, H.; Stafstrom, S.; Boman, M.; Sundgren, J. E. *Phys. Rev. Lett.* **1995**, *75*, 1336.
- Marsh, P. A.; Voet, A.; Mullens, T. J.; Price, L. D. *Carbon* **1971**, *9*, 797.
- Russ, J. C. *The Image Processing Handbook*, 3rd ed.; CRC Press: Boca Raton, 1999.
- Tang, C. C.; Bando, Y.; Golberg, D.; Xu, F. F. *Carbon* **2004**, *42*, 2625.
- Tuinstra, F.; Koenig, J. L. *J. Chem. Phys.* **1970**, *53*, 1126.
- Tuinstra, F.; Koenig, J. L. *J. Compos. Mater.* **1970**, *4*, 492.
- Cuesta, A.; Dhamelincourt, P.; Laureys, J.; Martinezalonso, A.; Tascon, J. M. D. *Carbon* **1994**, *32*, 1523.
- Cuesta, A.; Dhamelincourt, P.; Laureys, J.; Martinez-Alonso, A.; Tascon, J. M. D. *J. Mater. Chem.* **1998**, *8*, 2875.
- Nemanich, R. J.; Solin, S. A. *Phys. Rev. B* **1979**, *20*, 392.
- Wang, Y.; Alsmeyer, D. C.; McCreery, R. L. *Chem. Mater.* **1990**, *2*, 557.
- Livneh, T.; Haslett, T. L.; Moskovits, M. *Phys. Rev. B* **2002**, *66*.
- Kawashima, Y.; Katagiri, G. *Phys. Rev. B* **1995**, *52*, 10053.
- Hou, H. Q.; Jun, Z.; Weller, F.; Greiner, A. *Chem. Mater.* **2003**, *15*, 3170.
- Mazzetti, L.; Thistlethwaite, P. J. *J. Raman Spectrosc.* **2002**, *33*, 104.
- Pang, L. S. K.; Saxby, J. D.; Chatfield, S. P. *J. Phys. Chem.* **1993**, *97*, 6941.
- Jiang, W.; Nadeau, G.; Zaghib, K.; Kinoshita, K. *Thermochim. Acta* **2000**, *351*, 85.
- Christie, A. B. In *Methods of Surface Analysis*; Walls, J. M., Ed.; Cambridge Press University: Cambridge, 1989; p 136.
- McCreery, R. L. *Carbon Electrodes: Structural Effects on Electron-Transfer Kinetics*; Marcel Dekker: New York, 1991; Vol. 17, p 230.
- Choudhury, T.; Saied, S. O.; Sullivan, J. L.; Abbot, A. M. *J. Phys. D* **1989**, *22*, 1185.
- Handbook of X-ray Photoelectron Spectroscopy*; Chastain, J.; King, R. C., Eds.; Physical Electronics, Inc.: Eden Prairie, 1995; p 80.
- Sethuraman, A. R.; Stencil, J. M.; Rubel, A. M.; Cavin, B.; Hubbard, C. R. *J. Vac. Sci. Technol. A* **1994**, *12*, 443.
- Castignolles, M.; Loiseau, A.; Enouz, S.; Bernier, P.; Glerup, M. *Chem. Commun.* **2003**, 772, M3.8.1.
- Pels, J. R.; Kapteijn, F.; Moulijn, J. A.; Zhu, Q.; Thomas, K. M. *Carbon* **1995**, *33*, 1641.
- Stohr, B.; Boehm, H. P.; Schlögl, R. *Carbon* **1991**, *29*, 707.
- Poirier, D. M.; Weaver, J. H. *Surf. Sci. Spectra* **1994**, *2*, 232.
- Handbook of X-ray Photoelectron Spectroscopy*; Chastain, J.; King, R. C., Eds.; Physical Electronics, Inc.: Eden Prairie, 1995; p 40.
- Biniak, S.; Szymanski, G.; Siedlewski, J.; Swiatkowski, A. *Carbon* **1997**, *35*, 1799.
- Bard, A. J.; Faulkner, L. R. *Electrochemical Methods: Fundamentals and Applications*, 2nd ed.; John Wiley and Sons: New York, 2001; pp 211–216.
- Yang, H. H.; McCreery, R. L. *J. Electrochem. Soc.* **2000**, *147*, 3420.
- Xu, J.; Huang, W. H.; McCreery, R. L. *J. Electroanal. Chem.* **1996**, *410*, 235.
- Bard, A. J.; Faulkner, L. R. *Electrochemical Methods: Fundamentals and Applications*, 2nd ed.; John Wiley and Sons: New York, 2001; pp 236.
- The homogeneous equilibrium/kinetic rate constant and heterogeneous kinetic rate constant notation is as described in reference 57, p xiii.
- McIntyre, J. D. E. *J. Phys. Chem.* **1967**, *71*, 1196.
- Mao, L. Q.; Zhang, D.; Sotomura, T.; Nakatsu, K.; Koshiba, N.; Ohsaka, T. *Electrochim. Acta* **2003**, *48*, 1015.
- Goldstein, J. R.; Tseung, A. C. C. *J. Phys. Chem.* **1972**, *76*, 3646.
- McIntyre, J. D. E. *J. Phys. Chem.* **1969**, *73*, 4102.
- Gerlache, M.; Girousi, S.; Quarin, G.; Kauffmann, J. M. *Electrochim. Acta* **1998**, *43*, 3467.
- Khalil, L. B.; Girgis, B. S.; Tawfik, T. A. M. *J. Chem. Technol. Biotechnol.* **2001**, *76*, 1132.
- Venkatachalapathy, R.; Davila, G. P.; Prakash, J. *Electrochem. Commun.* **1999**, *1*, 614.
- Appleby, A. J.; Savy, M. *J. Electroanal. Chem.* **1978**, *92*, 15.
- Bielski, B. H. J.; Allen, A. O. *J. Phys. Chem.* **1977**, *81*, 1048.
- Jiang, S. P.; Lin, Z. G.; Tseung, A. C. C. *J. Electrochem. Soc.* **1990**, *137*, 759.
- Maldonado, S.; Morin, S.; Stevenson, K. J., manuscript in prep.
- Schulenburg, H.; Stankov, S.; Schuenemann, V.; Radnik, J.; Dorbandt, I.; Fiechter, S.; Bogdanoff, P.; Tributsch, H. *J. Phys. Chem. B* **2003**, *107*, 9034.
- Gruenig, G.; Wiesener, K.; Gamburzev, S.; Iliev, I.; Kaisheva, A. *J. Electroanal. Chem.* **1983**, *159*, 155.
- Wiesener, K. *Electrochim. Acta* **1986**, *31*, 1073.
- The Formation of Filamentous Carbon*; Baker, R. T. K.; Harris, P. S., Eds.; Marcel Dekker: New York, 1978; Vol. 14, p 147.
- Szymanski, G. S.; Grzybek, T.; Papp, H. *Catal. Today* **2004**, *90*, 51.
- Matzner, S.; Boehm, H. P. *Carbon* **1998**, *36*, 1697.
- Huang, M. C.; Teng, H. S. *Carbon* **2003**, *41*, 951.
- Leon, C. A. L. Y.; Solar, J. M.; Calemme, V.; Radovic, L. R. *Carbon* **1992**, *30*, 797.
- Mang, D.; Boehm, H. P.; Stanczyk, K.; Marsh, H. *Carbon* **1992**, *30*, 391.
- Strelko, V. V.; Kartel, N. T.; Dukhno, I. N.; Kuts, V. S.; Clarkson, R. B.; Odintsov, B. M. *Surf. Sci.* **2004**, *548*, 281.
- Maldonado, S.; Stevenson, K. J., manuscript in prep.